nature chemical engineering

Supplementary information

https://doi.org/10.1038/s44286-026-00443-7

Bioresorbable batteries for transient ingestible bioelectronics

In the format provided by the authors and unedited

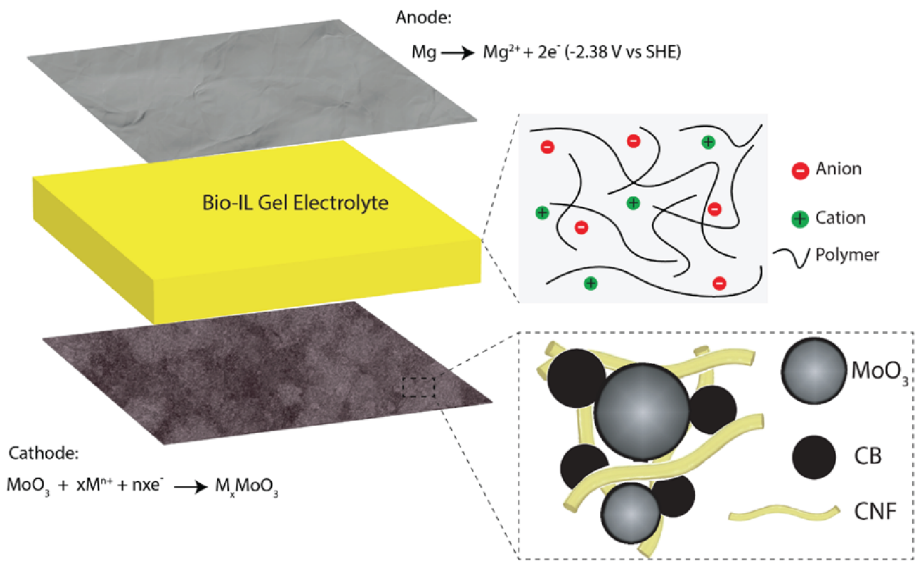
List of Contents:

Supplementary Figures 1-29

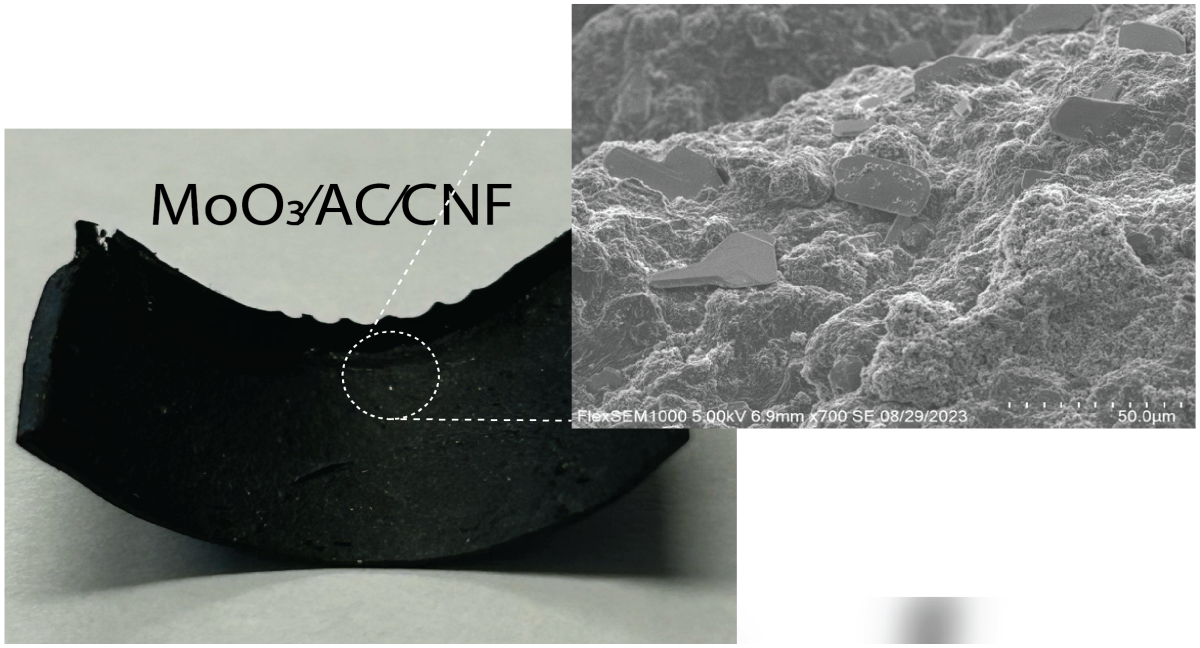
Supplementary Tables 1-3

Supplementary Note 1

Supplementary References



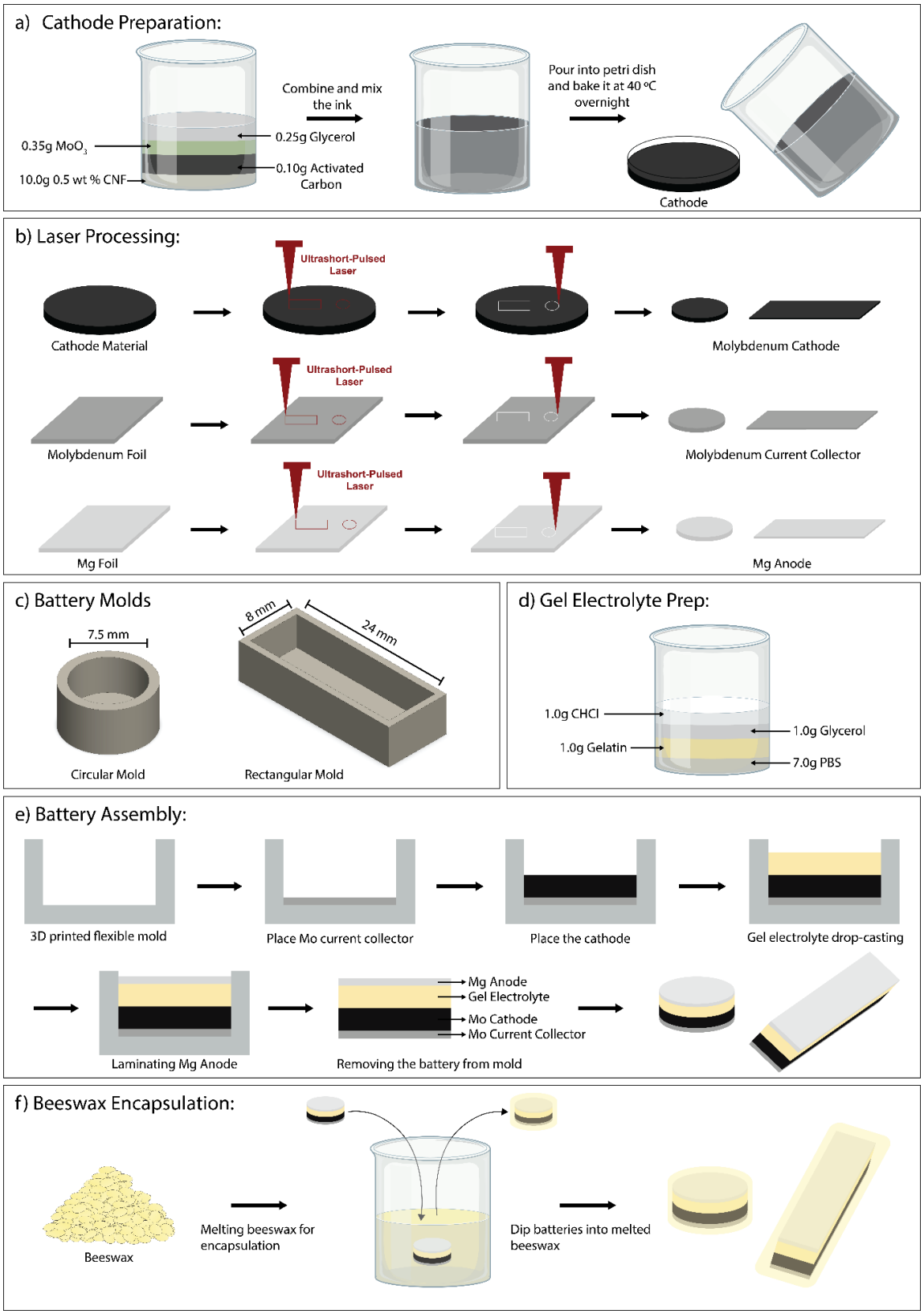
Supplementary Figure 1. Battery chemistry and components. The anodic reaction occurs, and Mg produces Mg^{+2} and cathodic reaction reduces O_2 in air ($Mg \rightarrow Mg^{+2} + 2e^-$). As for the cathode side, the reaction would be ($O_2 + 2H_2O + 4e^- \rightarrow 4OH^-$). For the selection of high capacitance cathode material, the reaction is ($MoO_3 + xM^{n+} + nxe^- \rightarrow MxMoO_3$).



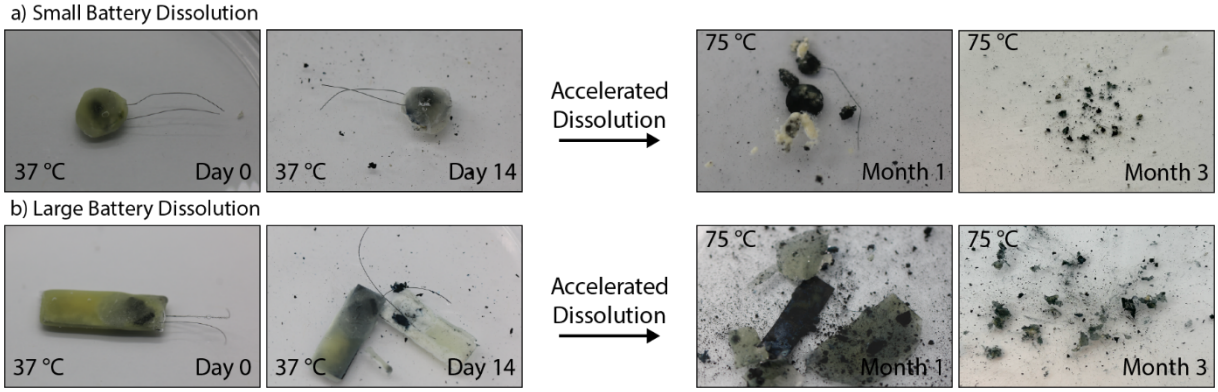
Supplementary Figure 2. Optical image and SEM image of paper electrode.



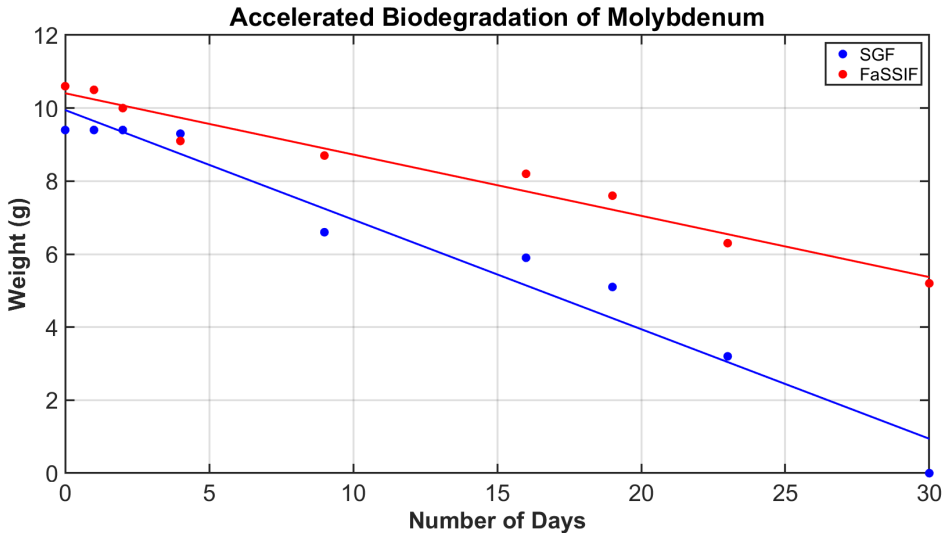
Supplementary Figure 3. ChCl: DL-LA based Bio-ionic liquid.



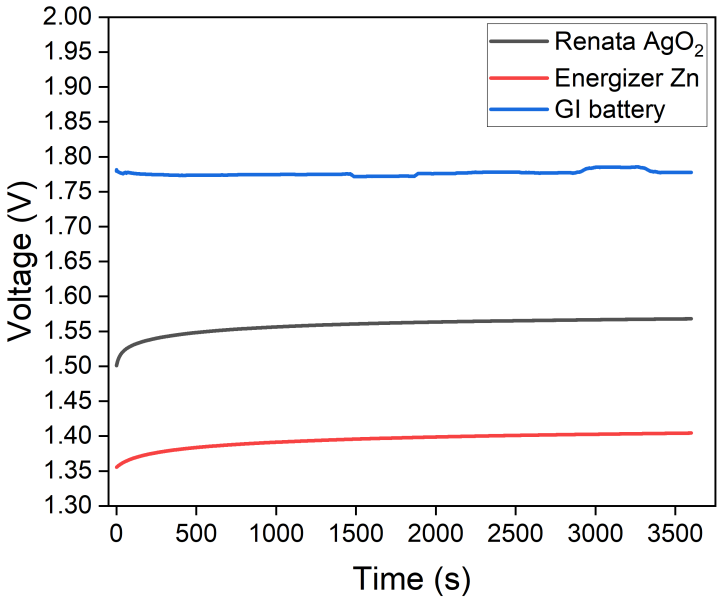
Supplementary Figure 4. Battery Fabrication and Assembly. a) Cathode preparation by mixing MoO_3, glycerol, activated carbon, and CNF, followed by drying at 40 °C. b) Laser processing of the cathode, current collector, and anode to cut pieces to size. c) Battery molds for shaping the final device. d) Preparation of the gel electrolyte by mixing choline chloride (CHCl), gelatin, glycerol, and PBS. e) Battery assembly by layering components inside the mold, and (f) Encapsulation with beeswax by dipping the assembled battery into molten wax.



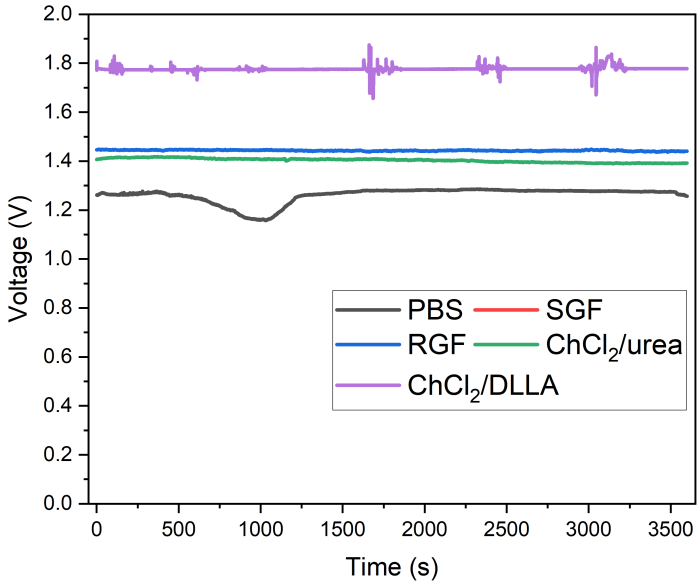
Supplementary Figure 5. Biodegradation of a) 000 size and b) the large battery. Samples remained in simulated gastric fluid (SGF) at 37 °C for 14 days, followed by accelerated dissolution at 75 °C up to 3 months.



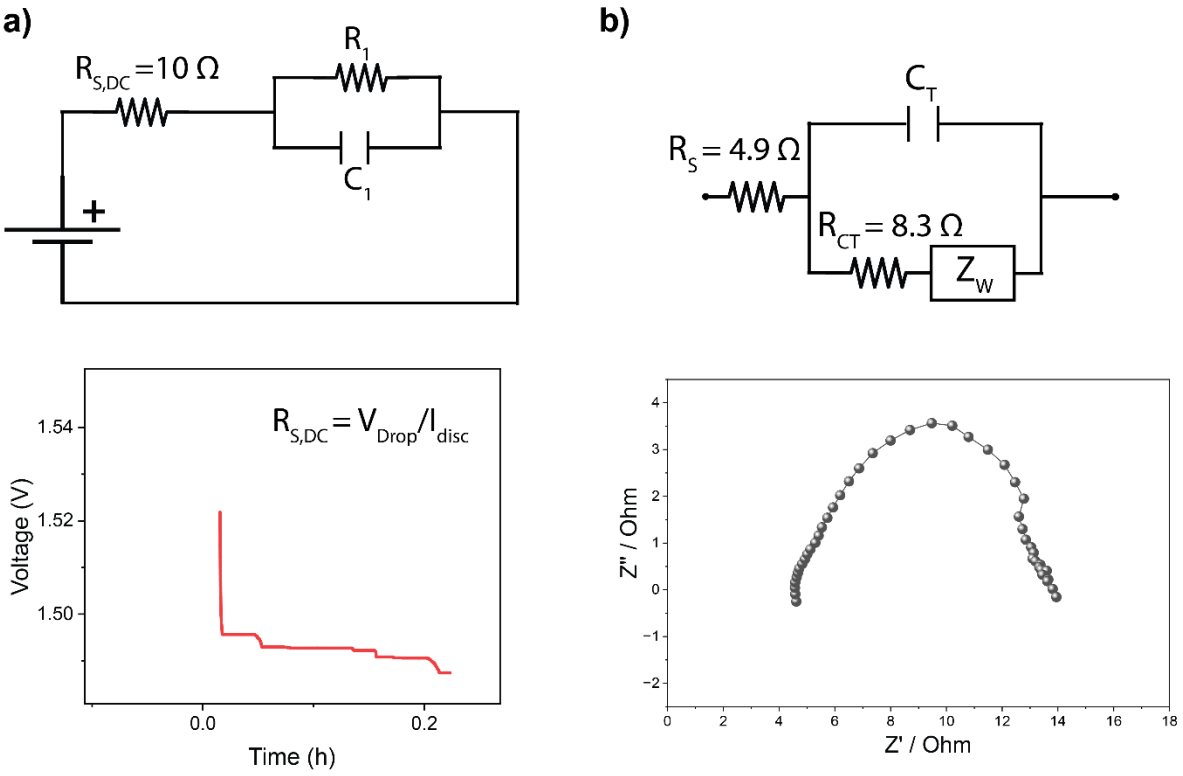
Supplementary Figure 6. Accelerated dissolution of Mo foil (25 µm) in both SGF and FaSSIF. Specifically, metallic molybdenum undergoes gradual oxidation in aqueous media to form soluble molybdate species, while MoO_3 can hydrolyze to yield molybdate ions, which represent the dominant and biologically relevant dissolution products. Equations related to the dissolution: $2Mo + 2H_2O + 3O_2 \rightarrow 2H_2MoO_4$ and $MoO_3 + H_2O \rightarrow 2OH^- + MoO_4^{2-}$



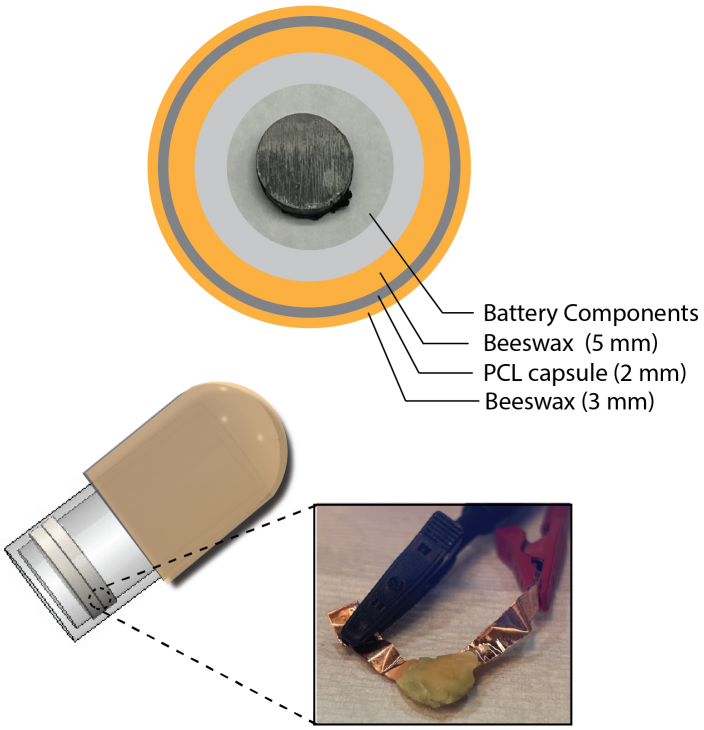
Supplementary Figure 7. 000- size battery OCV comparison with commercial capsule size batteries.



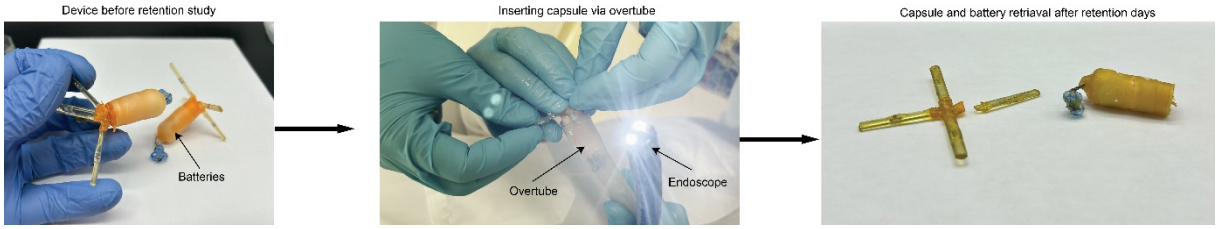
Supplementary Figure 8. Electrolyte OCV comparison. Open circuit voltage comparison of battery with different electrolyte materials in gel electrolyte. PBS: Phosphate buffered saline, RGF: Real gastric fluid, SGF: Simulated gastric fluid, ChCl: choline chloride, DLLA: DL- Lactic Acid.



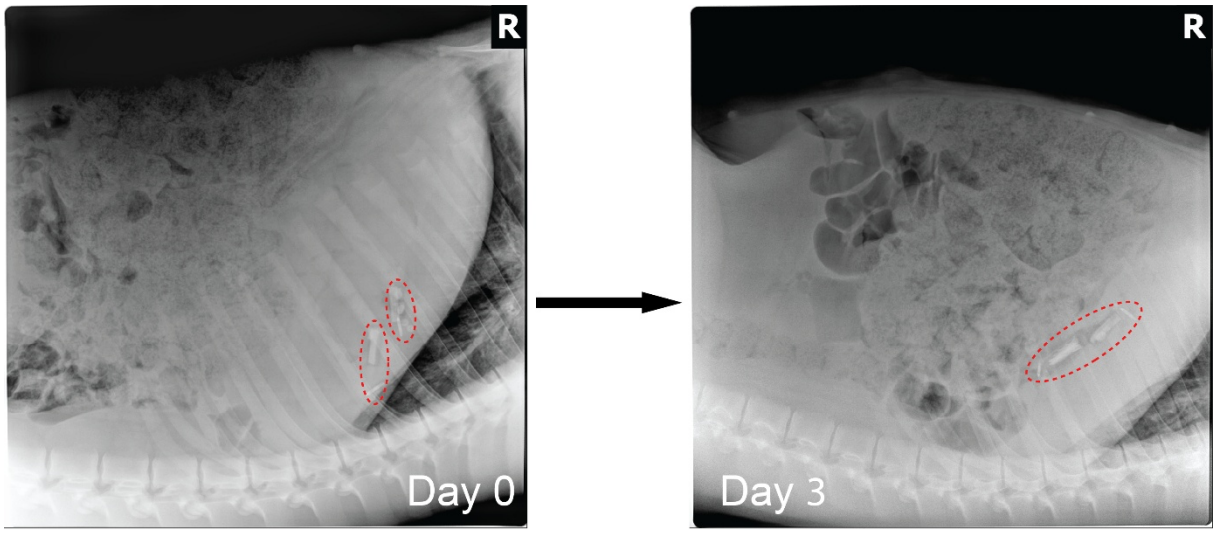
Supplementary Figure 9**.** Simplified DC battery model and impedance spectroscopy of biodegradable battery. a) First-order Thevenin equivalent circuit used for system-level representation of the biodegradable battery, consisting of an open-circuit voltage source (V_{OC}), series resistance (R_s), and a parallel RC element ($R_1 \parallel C_1$). b) Electrochemical impedance spectroscopy (EIS) Nyquist plot using a Randles equivalent circuit. The high-frequency intercept corresponds to the effective series resistance R_s, while the semicircle reflects the charge-transfer resistance and double-layer capacitance.



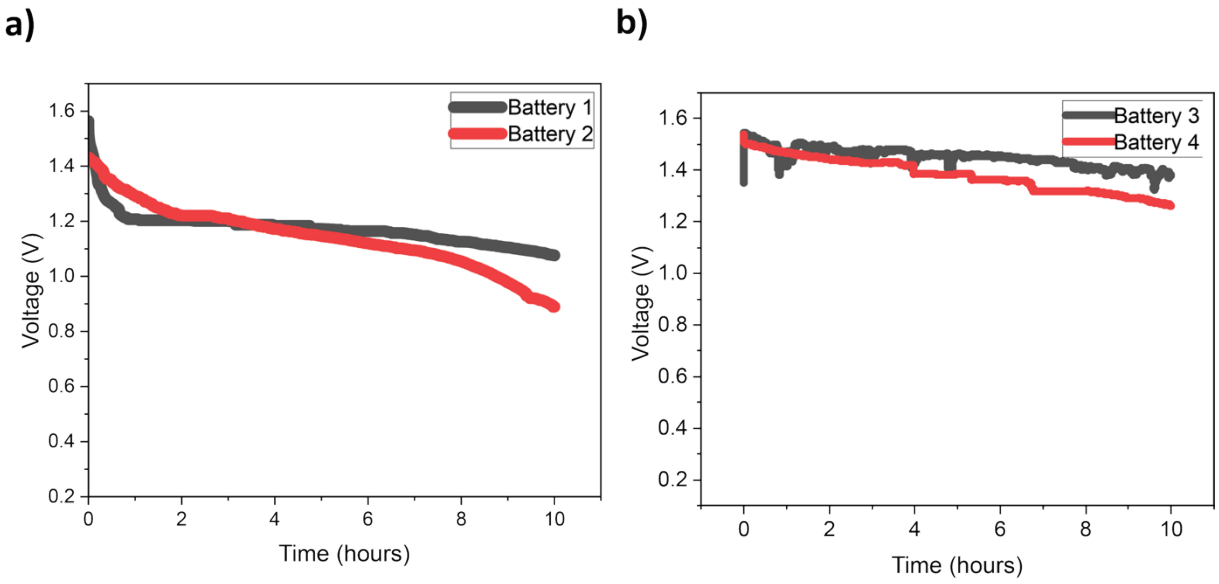
Supplementary Figure 10. Battery and capsule encapsulation layers using polymers and natural wax. Photograph shows the electrical connection of the retrieved 000-size battery after 3 days of stomach retention.



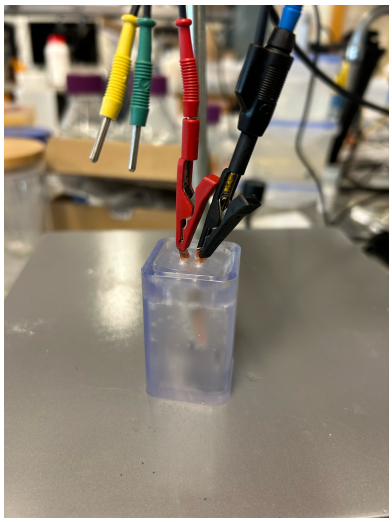
Supplementary Figure 11. Pictures of arm capsules, in vivo before and after.



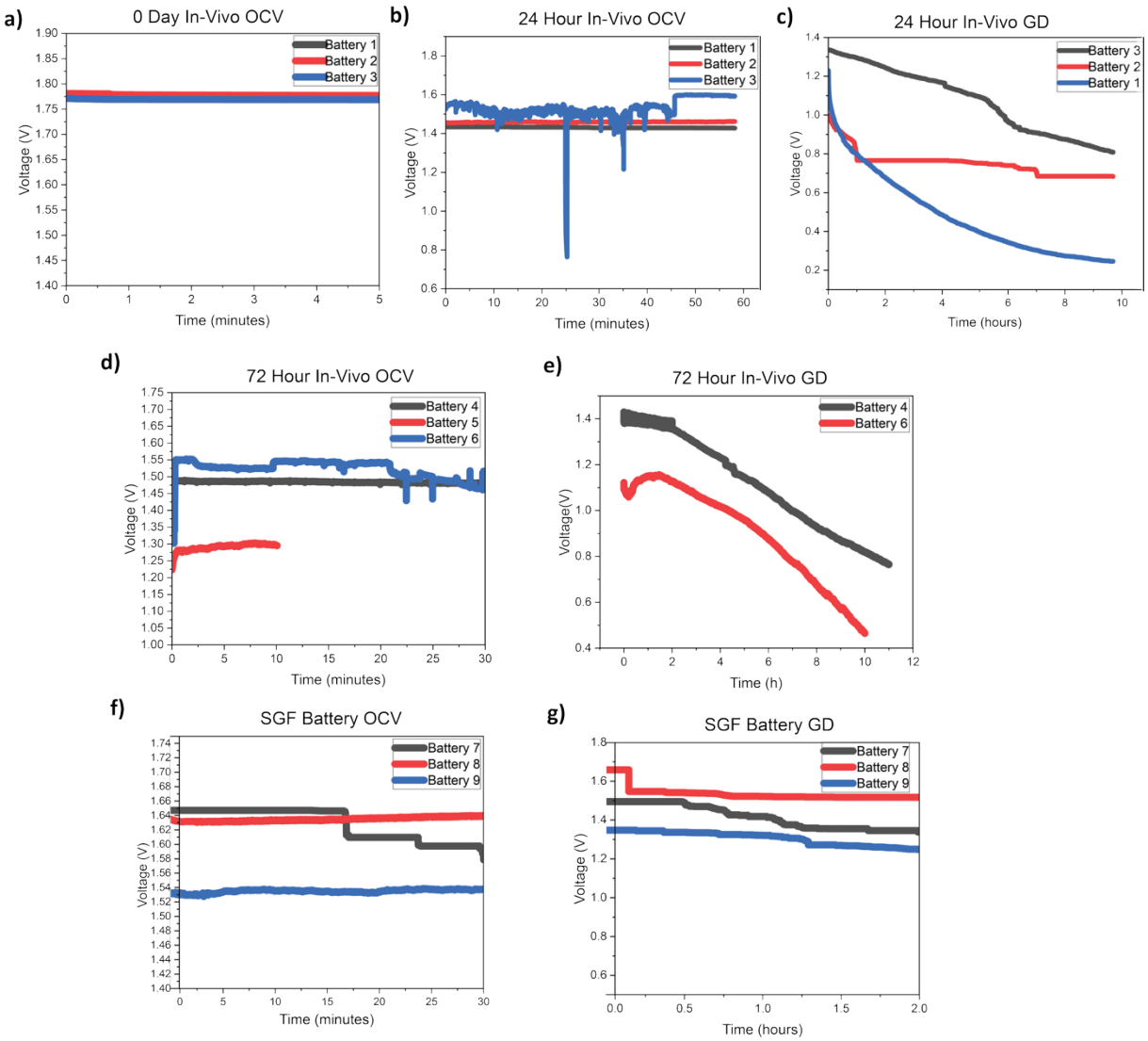
Supplementary Figure 12. X-Ray images of the large area batteries Day 0 and Day 3.



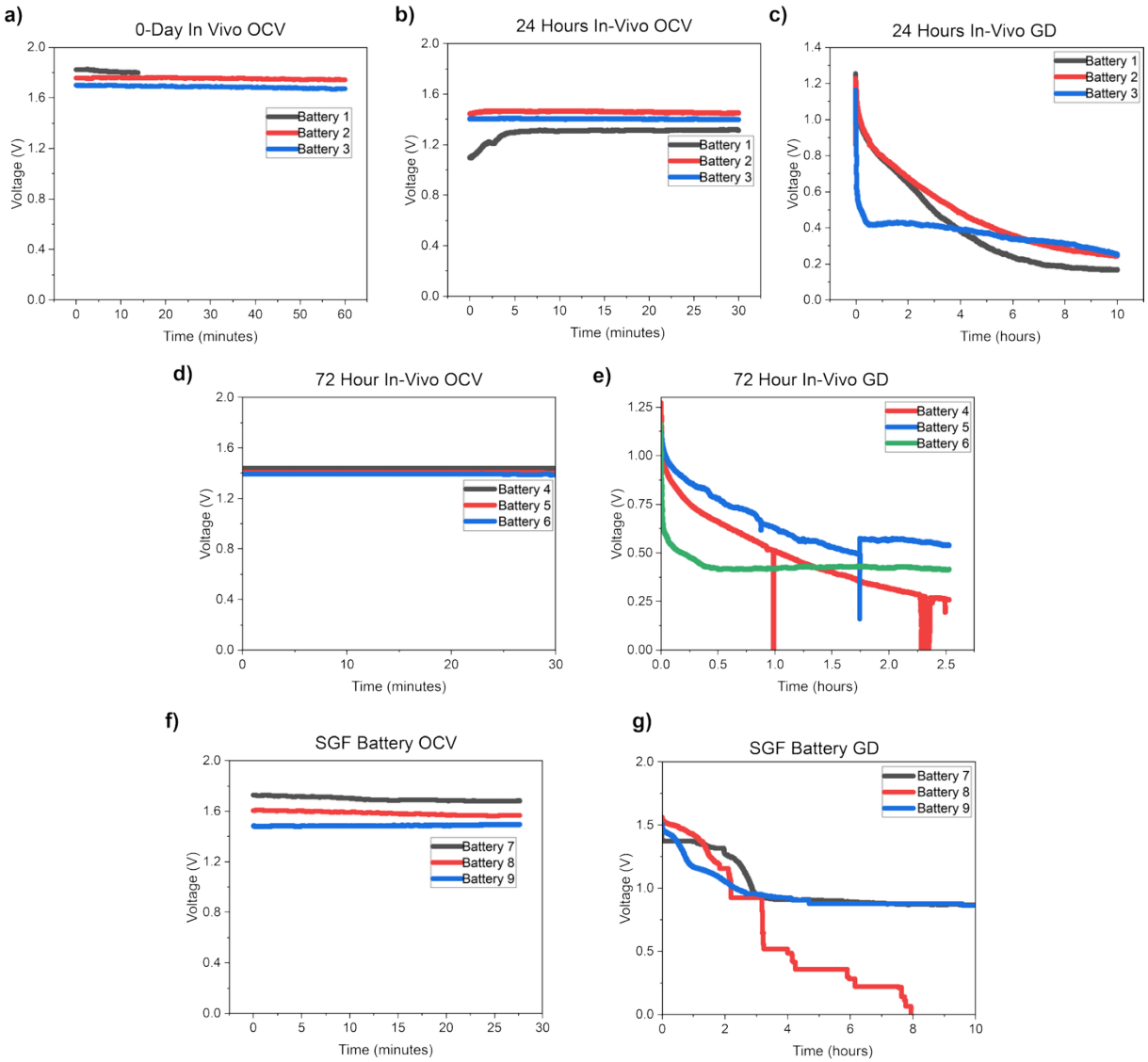
Supplementary Figure 13. Discharging curves for 000-size and large-area batteries at 0.1mA/cm^2.



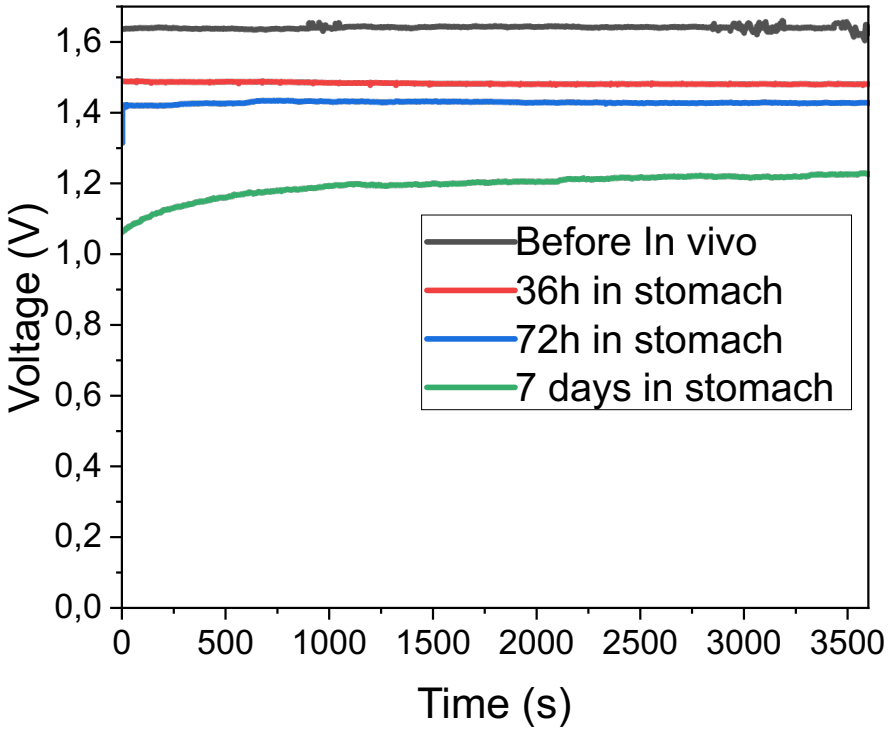
Supplementary Figure 14. Picture of a battery immersed in SGF while discharging and during open circuit voltage measurement.



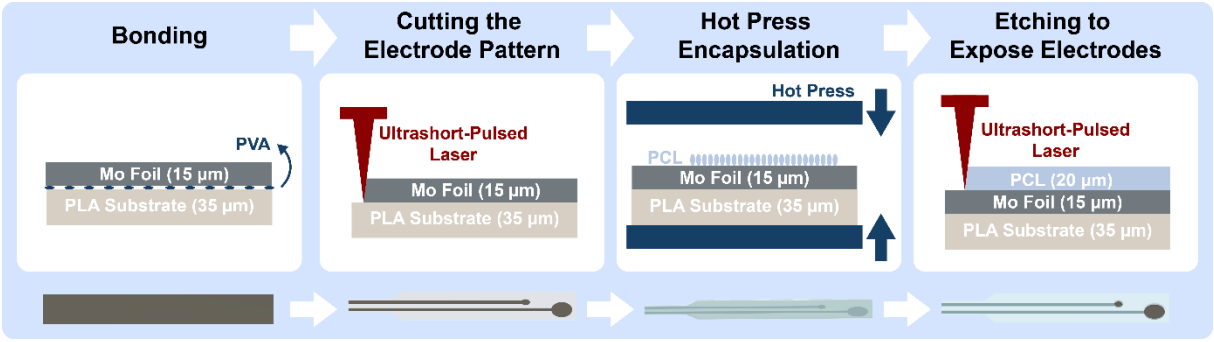
Supplementary Figure 15. Electrochemical characterization of 000-size batteries following gastric retention and simulated gastric fluid (SGF) immersion. a) Open-circuit voltage (OCV) measured at Day 0 prior to the 24 h in vivo gastric retention study. b) OCV and c) galvanostatic discharge (GD, 0.1 mA cm^{-2}) of batteries retrieved after 24 h of in vivo gastric retention. d) OCV measured after 72 h of in vivo gastric retention, followed immediately by e) galvanostatic discharge (Battery 5 discharge curve excluded due to complete depletion). f) OCV of batteries immediately after SGF immersion, followed by g) galvanostatic discharge. Different batteries were used for each retention and immersion condition (n = 9 total; n = 3 per condition).



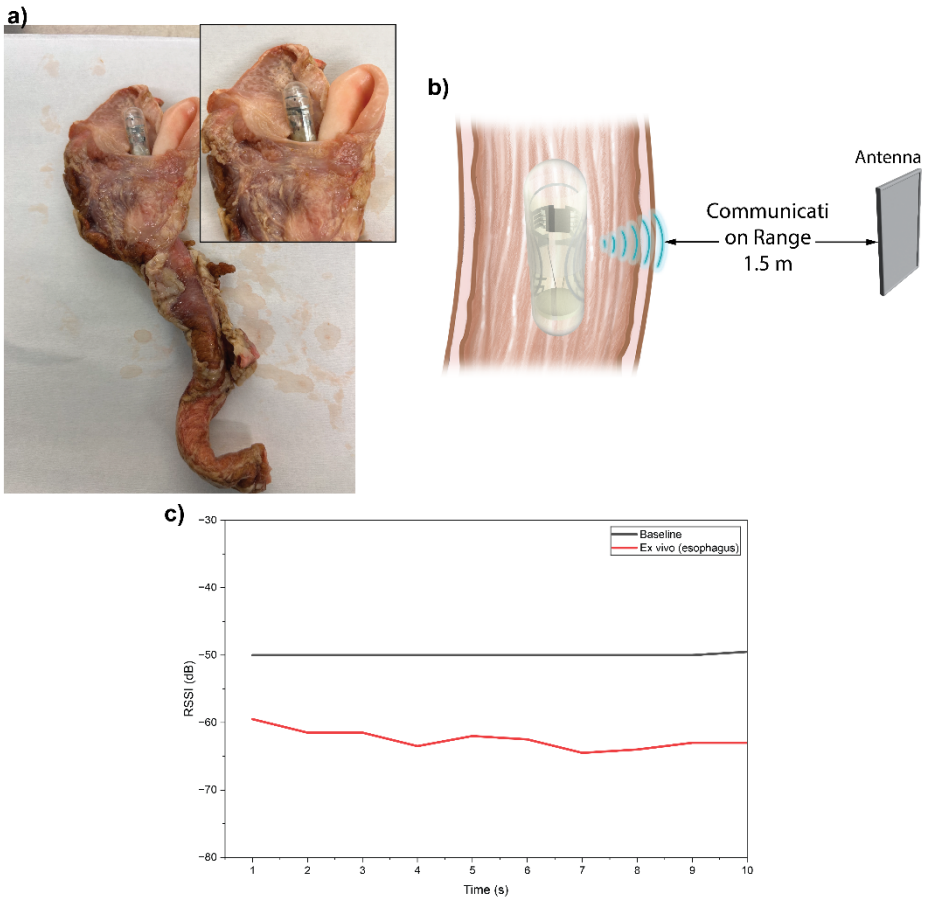
Supplementary Figure 16. Electrochemical characterization of large-area batteries following gastric retention and SGF immersion. a) OCV measured at Day 0 prior to the 24 h in vivo gastric retention study. b) OCV and c) galvanostatic discharge (GD, 0.1 mA cm^{-2}) of batteries retrieved after 24 h of in vivo gastric retention. d) OCV measured after 72 h of in vivo gastric retention, followed immediately by (e) galvanostatic discharge. f) OCV of batteries immediately after SGF immersion, followed by (g) galvanostatic discharge. Different batteries were used for each retention and immersion condition (n = 9 total; n = 3 per condition).



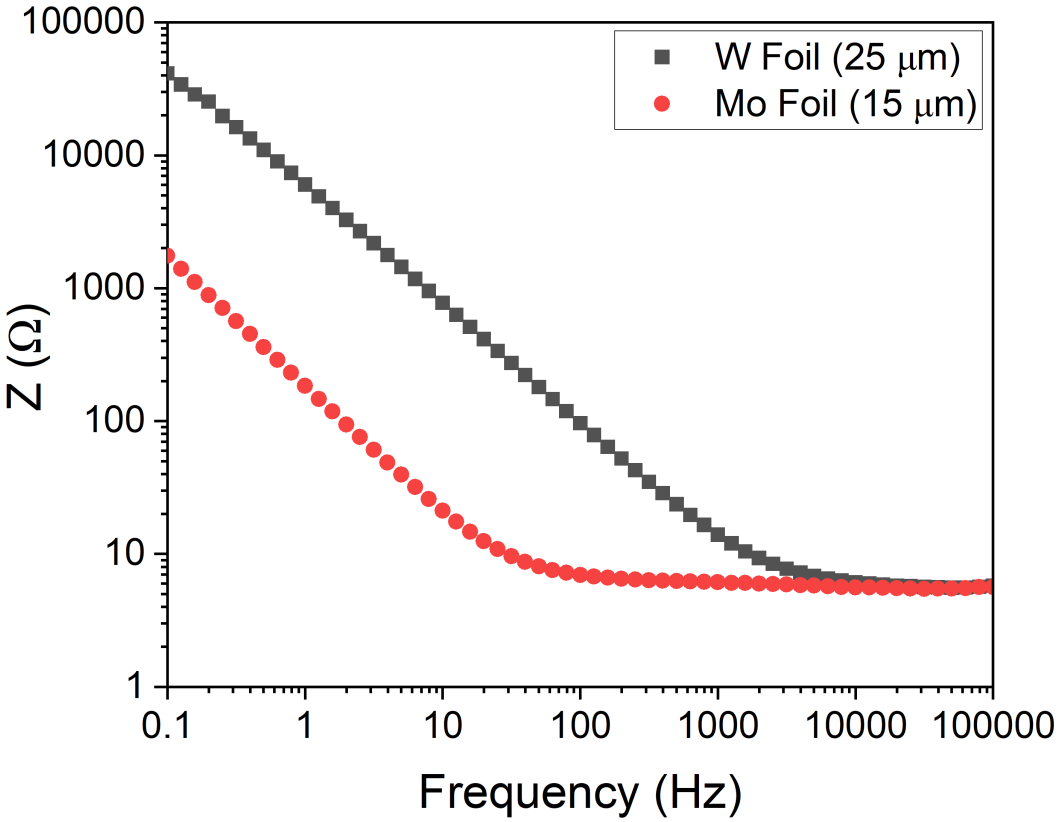
Supplementary Figure 17. In vivo retention and open-circuit voltage (OCV) comparison at multiple time points. OCV measured before in vivo placement (Day 0) and after 36 h, 72 h, and 7 days of gastric retention.



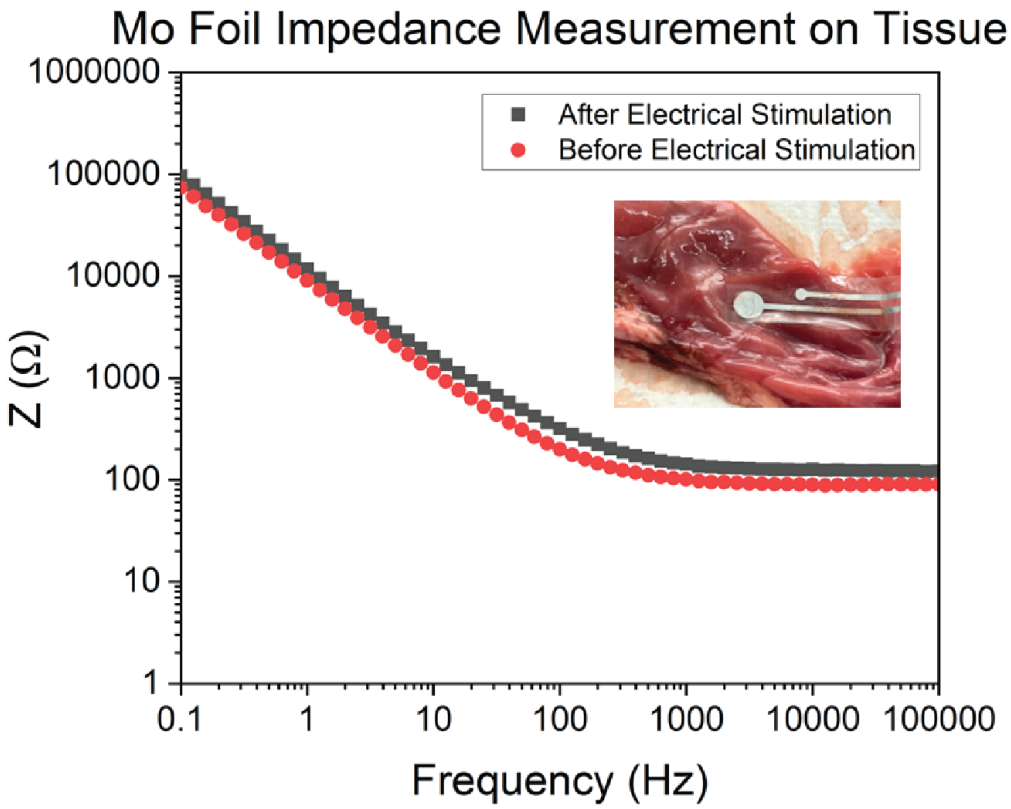
Supplementary Figure 18. Details of Mo electrode and RFID antenna fabrication.



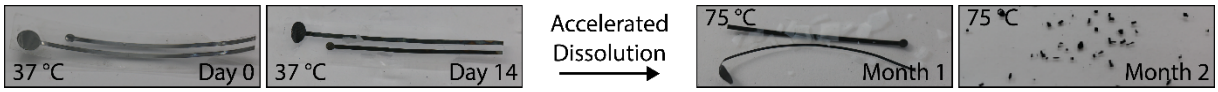
Supplementary Figure 19. Ex vivo performance of the biodegradable, battery assisted RFID tag. a) Optical images of the ex vivo esophagus and BA-RFID tag encapsulated in a 000 gelatin capsule. b) Schematic representation of the RSSI measurement through the ex vivo swine esophagus. c) RSSI measurements recorded from a device through ex- vivo tissue.



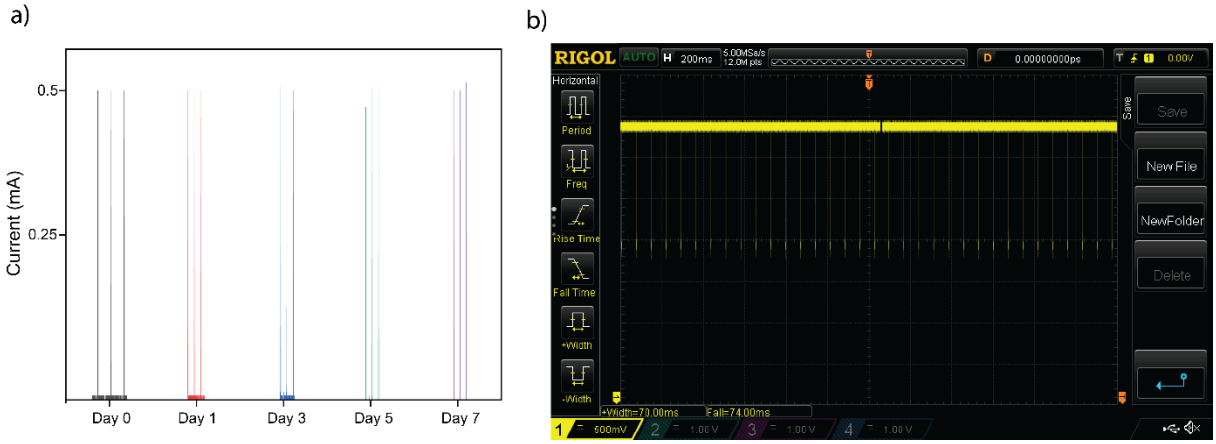
Supplementary Figure 20. Impedance spectroscopy of 15 μm thick Mo and W films in SGF. ($Z_{Mo,\ 14\ Hz}$ = 18.3 Ω; $Z_{W,\ 14\ Hz}$ = 700 Ω)



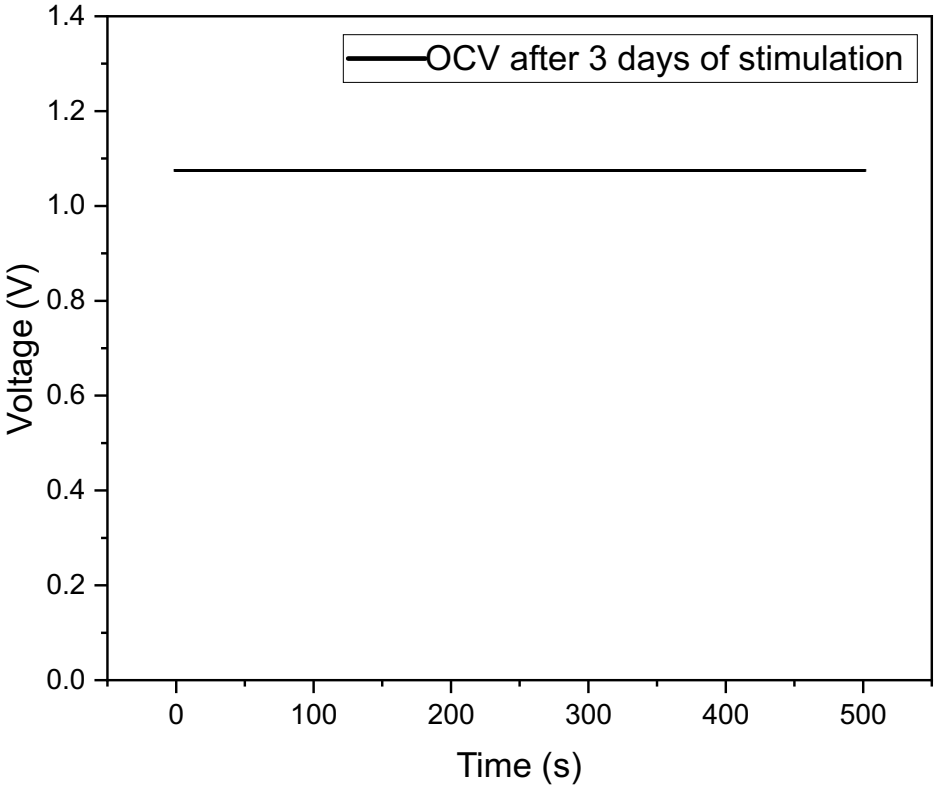
Supplementary Figure 21. Ex vivo tissue impedance spectroscopy of Mo electrode before and after stimulation on gastric tissue (20 minutes, 0.5 mA, 14 Hz), ($Z_{before,\ 14\ Hz}$ = 856.3 Ω; $Z_{after,\ 14\ Hz}$ = 1252.1 Ω)



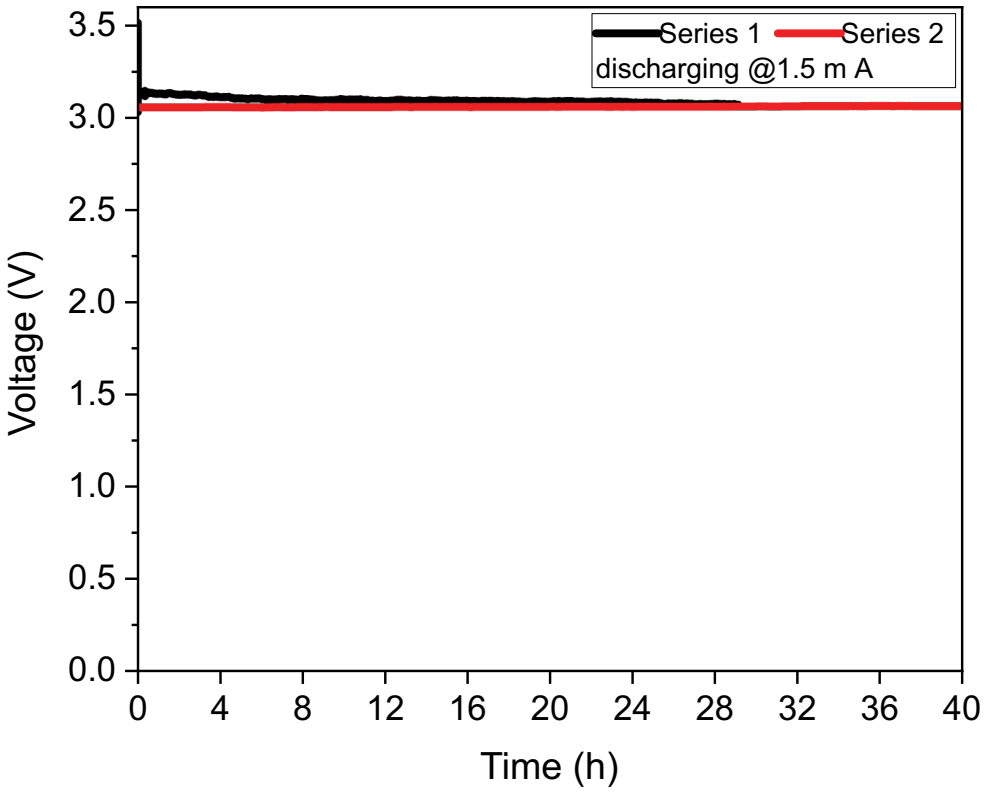
Supplementary Figure 22. Biodegradation of the electrode in simulated gastric fluid at 37 °C for 14 days, followed by accelerated dissolution in 75 °C up to 2 months.



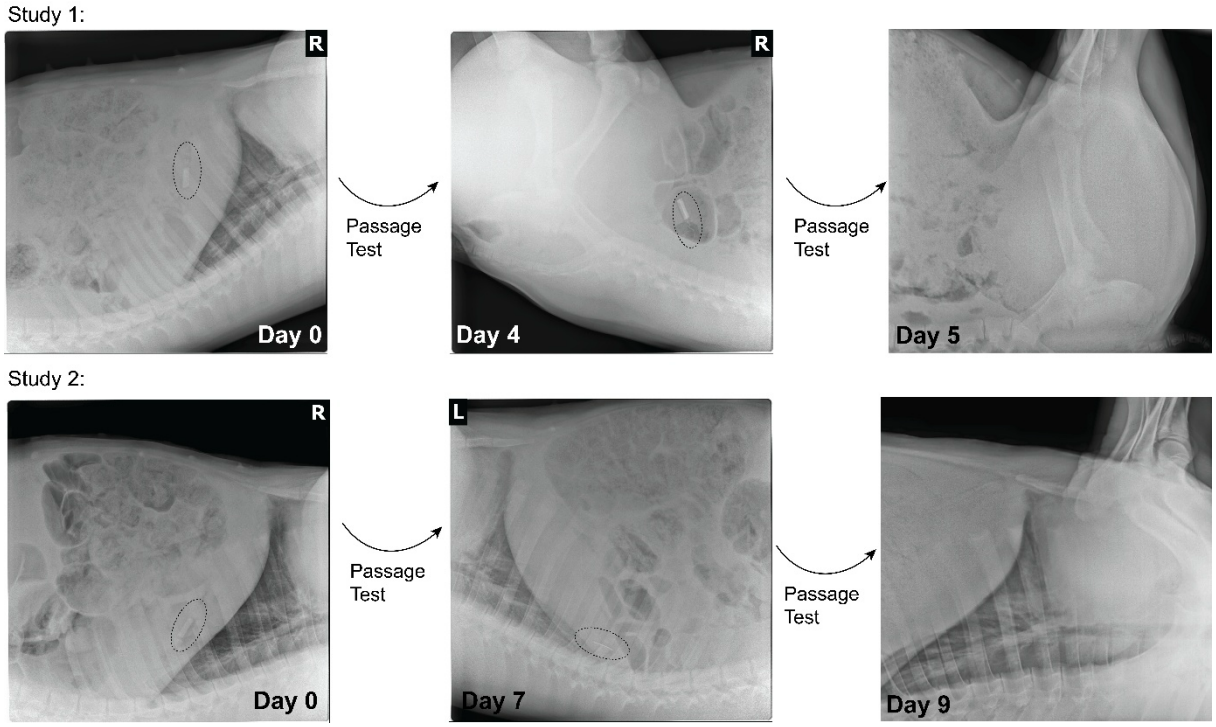
Supplementary Figure 23. a) Output signal of the stimulation PCB, powered by 2 batteries in parallel, b) Sample output signal picture from oscilloscope screen on day 3.



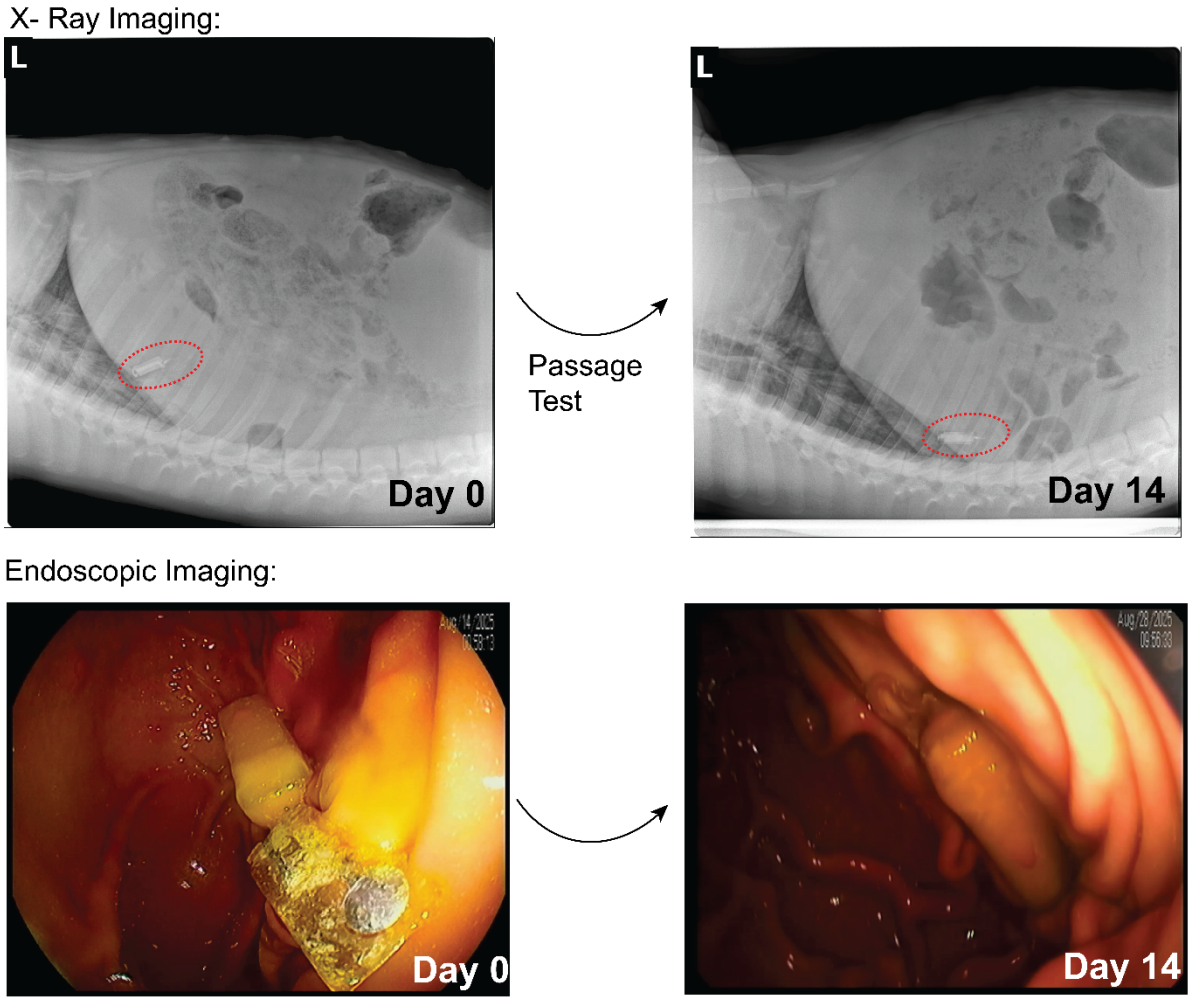
Supplementary Figure 24. Large area battery OCV after 3 days of continuous stimulation.



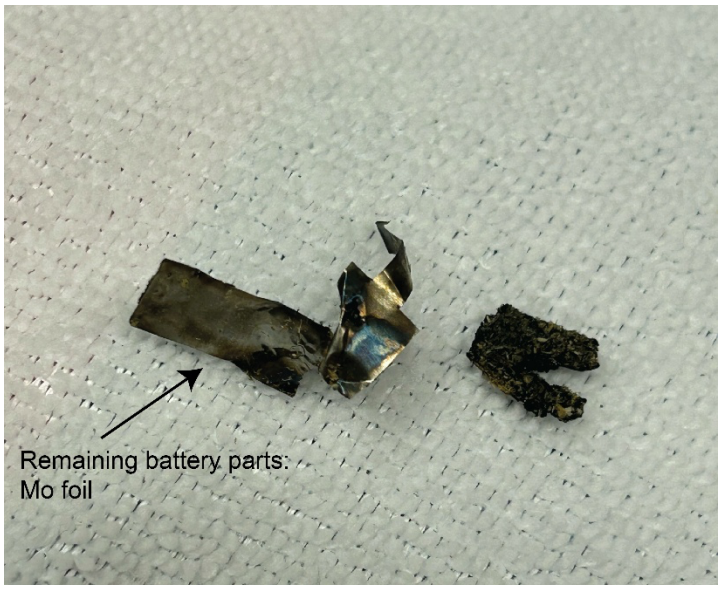
Supplementary Figure 25. Discharging curve of 2-series connected batteries at a current of 1.5 mA.



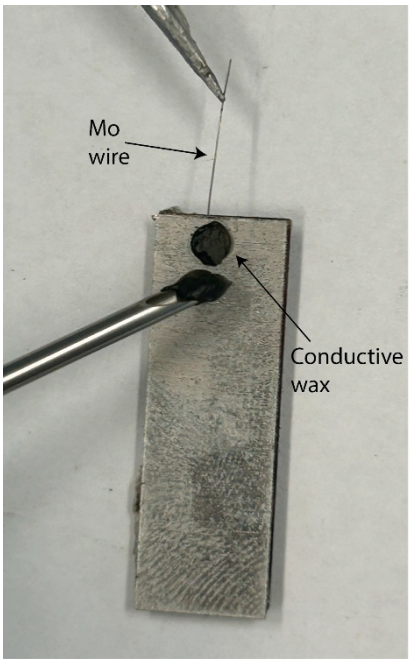
Supplementary Figure 26. X-ray images of the GES capsule for safe passage test.



Supplementary Figure 27. Two weeks long passage test. The device location in the stomach confirmed using X-Ray and endoscopy imaging.



Supplementary Figure 28. Battery parts excreted after the passage test, day 18.



Supplementary Figure 29. Battery connection with bioresorbable wax and interconnect

Supplementary Table 1. The biodegradation rates and daily intake amounts of the materials used in the capsule devices reported in this work (bw: body weight). Large-area batteries utilize 85 mg Mg, 20 mg Mo, 71 mg MoO_3, 10 mg cellulose, and 52 mg of bio-IL.

	Materials	**Degradation Rate (PBS, 37 °C)**	**Daily Intake**
Metals	Mg	12 μm/day[1]	420 mg (recommended)
	Mo	0.02 μm/day[2]	2 mg [3] (recommended) 40 mg/kg/day[4] (no toxicity)
	Activated Carbon	Not specified	0.5–1 g kg^{-1} [5]
Polymers	Cellulose	Not specified	660–900 mg kg^{-1} [5]
	PCL	0.5-2 years	Not specified
Natural Wax	Beeswax	Not specified	22 mg/kg/bw/day[6]
	Candelilla wax	Not specified	600 mg/kg/bw/day[7]

Supplementary Table 2. Comparison table with the reported bioresorbable/biodegradable batteries.

Reference	**Battery Type**	**Voltage**	**Power**	**Capacity**	**Energy Density**
Huang. et.al., 2023[8]	Zn	0.7 V	6 μW	1.728 mWh	-
Jia et.al.,2016[9]	Mg	1.75 V	64.6 μW cm^{-2} (80 μA/cm^2)	3.79 mAh cm^{-2} (10 μA/cm^2)	4.70 mWh/cm^2
Karami-Mosammam et.al.,2022[10]	Mg	1.7 V	196 μW/cm^2	4.7 mAh (45 μA/cm^2)	1.72 mWh/ cm^2
Huang et.al., 2018[11]	Mg	1.6 V	0.27 mW/cm^2	6.5 mAh (12.5 μA/cm^2)	6.5 mWh/cm^2
Bandodkar et.al.,2020[12]	Mg	1.8 V	-	3 mAh (1 mA)	-
This work	**Mg**	**1.84 V**	**239 μW/cm^2**	**3.5 mAh 3.5 mAh/cm^2 (0.2mA/cm^2) ($V_{Cut-off}$=0.8 V)**	**4.13 mWh/cm^2**
Huang et.al., 2022[1]	Mg-I_2	1.8 V	0.7 mW cm^{-2}	2.45 mAh 9.8 mAh cm^{-2} (0.4 mA cm^{-2}) ($V_{Cut-off}$= 1.2V)	17.7 mWh/cm^2

Supplementary Table 3. Comparison of device applications of biodegradable batteries.

Reference	**Type**	**Application**	**Device**	**Connection**	**Translational**
Huang. et.al., 2022[1]	Bioresorbable battery	Cardiac Pacing	Implant	Wireless	In vivo mice
Karami-Mosammam et.al.,2022[10]	Bioresorbable battery	Electrochemical Sensor	Wearables	Wireless	Wearable Patch
Huang et.al., 2023[8]	Bioresorbable battery	Modulation of cell behavior	Implant	-	In vitro, in vivo rats
Bandodkar et.al.,2020[12]	Biodegradable battery	Hearth rate sensor	Wearables	Wireless	Wearable Patch
Rezaie et.al., 2023[13]	Biocompatible battery	Self-powered	Ingestible	-	-
This work	Bioresorbable battery	Electroceuticals, sensor	Ingestible	Wireless	In vivo Large Animal

Supplementary Note 1: RFID Antenna Design, Simulation and Link Budget Analysis

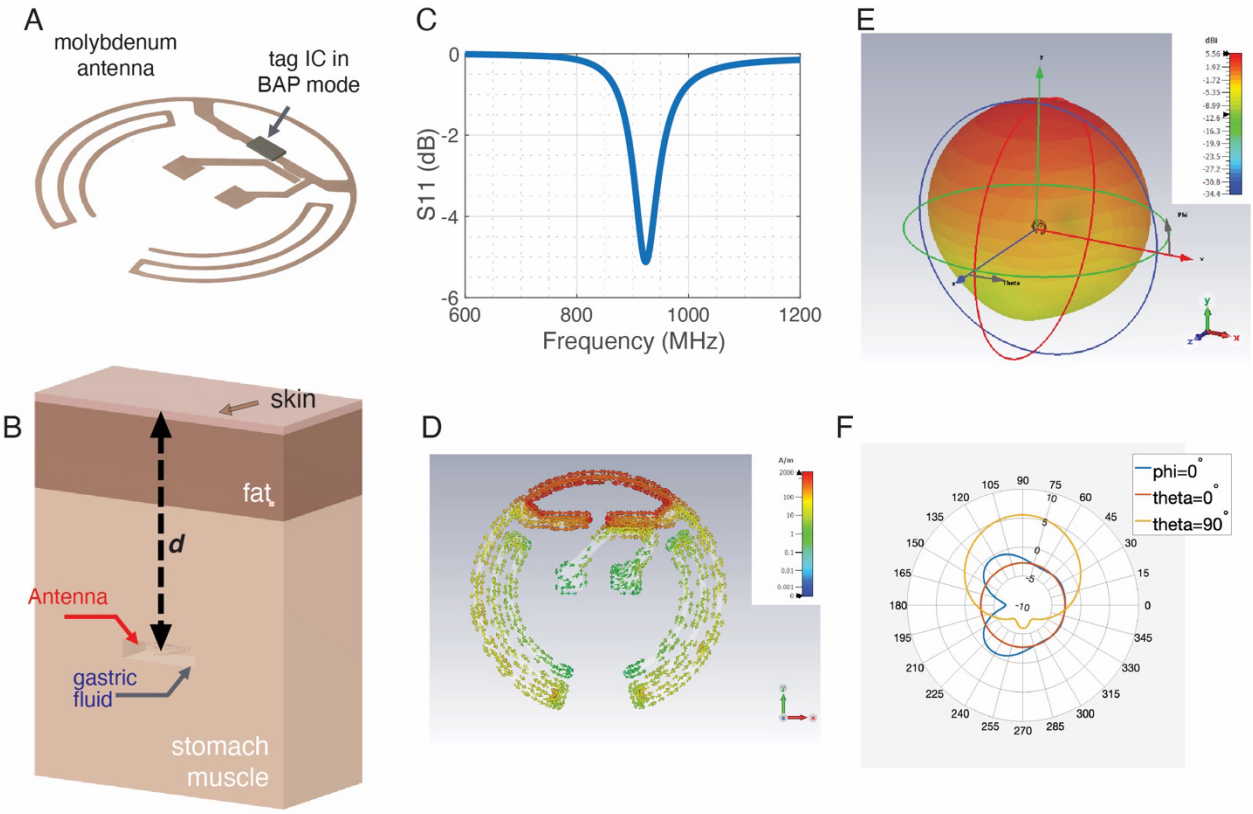


Figure 30. CST full-wave electromagnetic simulation results of a custom 915 MHz molybdenum ingestible antenna. (A) The antenna utilizes molybdenum for the antenna and a tag IC chip. (B) The simulations include a GI tract tissue model comprising a 2 mm skin layer and 30 mm of fat, with the antenna placed 15 cm (d) below the skin surface and immersed in gastric fluid and stomach muscle tissue. The tissue properties are cited from [14]. (C) illustrates the simulated S11 parameter of the antenna. Surface current distribution at the resonant frequency is shown in (D), while 3D and 2D far-field radiation patterns are shown in (E) and (F), respectively.

Link Budget Analysis: The link budget is decomposed into two independent one-way links, as is appropriate for an active backscatter architecture in which the tag is battery-assisted and actively drives its return transmission, thereby eliminating the round-trip path-loss penalty of passive backscatter systems. The reader antenna gain is 9 dBi on both transmit and receive, the simulated tag antenna directivity is −2 dBi at minimum (from Figure 30F), and the reader transmit power is 15 dBm. The 4 m separation between the skin surface and the external reader is treated as an air-only path, with tissue loss applied as a separate additive term. The free-space path loss over 4 m at 915 MHz is computed as:

$$FSPL = * 20 \cdot \log(4\pi R) = 43.7 \text{ dB}$$

For the downlink, the power delivered to the tag chip is,

$$P_{rx\_tag} = P_t + G_{reader} + P_{tag} - FSPL - L_{tissue}$$

$$= 15 + 9 + (-2) - 43.7 - 2.37 = -24.1 \text{ dBm}$$

The EM4325 in BAP mode at its most sensitive setting has a minimum read/write sensitivity of −31 dBm, yielding an activation margin of +6.9 dB — sufficient for reliable tag wake-up at this range.

For the uplink, the power received at the reader is

$$P_{rx\_reader} = EIRP_{tag} + G_{reader} - FSPL - L_{tissue}$$

$$= (-2) + 9 - 43.7 - 2.37 = -39.1 \text{ dBm}$$

The effective noise floor at the reader receiver is

$$N = 174 \frac{dBm}{Hz} + NF + 10\, logB(Hz)$$

Where dBm is thermal noise at room temperature, NF is the Noise Figure in dB, and B is the system bandwidth in Hz,

$$N = -127 + 5 = -122\, dBm$$

$N = -122$ dBm giving an uplink SNR margin of −39.1 − (−122) = +82.9 dB, which is more than sufficient for error-free demodulation even in the presence of orientation-dependent amplitude variations and multipath effects.

References

[1] I. Huang, Y. Zhang, H. M. Arafa, S. Li, A. Vazquez-Guardado, W. Ouyang, F. Liu, S. Madhvapathy, J. W. Song, A. Tzavelis, J. Trueb, Y. Choi, W. J. Jeang, V. Forsberg, E. Higbee-Dempsey, N. Ghoreishi-Haack, I. Stepien, K. Bailey, S. Han, Z. J. Zhang, C. Good, Y. Huang, A. J. Bandodkar, J. A. Rogers, *Energy Environ. Sci.* **2022**, *15*, 4095.

[2] G. Lee, E. Ray, H.-J. Yoon, S. Genovese, Y. S. Choi, M.-K. Lee, S. Şahin, Y. Yan, H.-Y. Ahn, A. J. Bandodkar, J. Kim, M. Park, H. Ryu, S. S. Kwak, Y. H. Jung, A. Odabas, U. Khandpur, W. Z. Ray, M. R. MacEwan, J. A. Rogers, *Sci. Adv.* **2022**, *8*, eabp9169.

[3] S. M. Hays, K. Macey, D. Poddalgoda, M. Lu, A. Nong, L. L. Aylward, *Regulatory Toxicology and Pharmacology* **2016**, *77*, 223.

[4] F. Jay Murray, R. W. Tyl, F. M. Sullivan, A. K. Tiwary, S. Carey, *Reproductive Toxicology* **2014**, *49*, 202.

[5] A. S. Sharova, F. Melloni, G. Lanzani, C. J. Bettinger, M. Caironi, *Adv Materials Technologies* **2021**, *6*, 2000757.

[6] E. F. S. Authority (EFSA), *EFSA Journal* **2007**, *5*, 615.

[7] EFSA Panel on Food Additives and Nutrient Sources added to Food (ANS), *EFSA Journal* **2012**, *10*, 2946.

[8] X. Huang, H. Hou, B. Yu, J. Bai, Y. Guan, L. Wang, K. Chen, X. Wang, P. Sun, Y. Deng, S. Liu, X. Cai, Y. Wang, J. Peng, X. Sheng, W. Xiong, L. Yin, *ACS Nano* **2023**, *17*, 5727.

[9] X. Jia, C. Wang, C. Zhao, Y. Ge, G. G. Wallace, *Adv Funct Materials* **2016**, *26*, 1454.

[10] M. Karami-Mosammam, D. Danninger, D. Schiller, M. Kaltenbrunner, *Advanced Materials* **2022**, *34*, 2204457.

[11] X. Huang, D. Wang, Z. Yuan, W. Xie, Y. Wu, R. Li, Y. Zhao, D. Luo, L. Cen, B. Chen, H. Wu, H. Xu, X. Sheng, M. Zhang, L. Zhao, L. Yin, *Small* **2018**, *14*, DOI 10.1002/smll.201800994.

[12] A. J. Bandodkar, S. P. Lee, I. Huang, W. Li, S. Wang, C.-J. Su, W. J. Jeang, T. Hang, S. Mehta, N. Nyberg, P. Gutruf, J. Choi, J. Koo, J. T. Reeder, R. Tseng, R. Ghaffari, J. A. Rogers, *Nat Electron* **2020**, *3*, 554.

[13] M. Rezaie, Z. Rafiee, S. Choi, *Advanced Energy Materials* **2023**, *13*, 2202581.

[14] https://itis.swiss/virtual-population/tissue-properties/database/dielectric-properties/